Bio-Medical Materials and Engineering 26 (2015) S1381–S1388
DOI 10.3233/BME-151436
IOS Press

Static imaging of the electrical impedance tomography on cylinder physical phantom

Ruigang Liu[a], Feng Fu[b], Fusheng You[a], Xuetao Shi[b] and Xiuzhen Dong[b,*]
[a]*Department of Medical Imaging, School of Biomedical Engineering, Fourth Military Medical University, Xi'an, 710032, China*
[b]*Department of Medical Electronic Engineering, School of Biomedical Engineering, Fourth Military Medical University, Xi'an, 710032, China*

Abstract. Static imaging of the electrical impedance tomography can obtain the absolute electrical conductivity distribution at one section of the subject. The test is performed on a cylinder physical phantom in which slim rectangle, hollow cylinder, small rectangle or three cylinders are selected to simulate complex conductivity perturbation objects. The measurement data is obtained by a data acquisition system with 32 compound electrodes. A group of static images of conductivity distribution in the cylinder phantom are reconstructed by the modified Newton-Raphson algorithm with two kinds of regularization methods. The results show correct position, size, conductivity difference, and similar shape of the perturbation objects in the images.

Keywords: Electrical impedance, tomography, reconstruction algorithm, physical phantom, static imaging

1. Introduction

Electrical impedance tomography can obtain the electrical impedance distribution image in the section of electrodes array by injecting alternative current and detecting the response voltages on the surface of a human body. For the characteristics of non-invasion, free radiation, and repeatability, EIT shows huge prospect in biomedical application, such as edema [1], hemorrhage or bleeding [2], and lung ventilation [3-5]. There are two procedures in the reconstruction algorithm, one is the forward problem and the other is the inverse problem. Most of the forward problem is solved by the finite element method (FEM) [6, 7] and some literatures use the boundary element method (BEM) [8, 9]. There are many methods to solve the inverse problem, such as Newton-Raphson algorithm [10, 11], expectation maximum method [12], and so on. In order to reduce the ill-posed problem, regularization method, for example Tikhonov method [13], SVD method [14], and L1 norm method [15], is necessary to be applied during the procedure of solving the inverse problem. Electrodes are the sensors of EIT. Usually, the more the number of electrodes is, the better the quality of reconstruction images is [16]. Numerical model [17], physical phantom [18, 19], and animal model [20, 21] are valid tools to

*Address for correspondence: Xiuzhen Dong, Department of Medical Electronic Engineering, School of Biomedical Engineering, Fourth Military Medical University, 169#, Changle West Road, Xi'an, 710032, China. Tel.: +86 29 84776397; Fax: +86 29 84776397; E-mail: dongyang@fmmu.edu.cn.

verify the performance of EIT algorithm and system.

According to the property of reconstructed electrical impedance, EIT can be divided into two kinds. Difference EIT or dynamic EIT aims to reconstruct the conductivity distribution variation using two frames measurement data at different times or frequencies. Static EIT aims to reconstruct the absolute conductivity distribution using one frame measurement data at one time and frequency. Difference EIT is a popular selection for less system error from the difference of data. To some extent, Static imaging is the final goal of EIT.

In this paper, all of the measurement data are acquired by EIT data acquisition system with 32 compound electrodes on a cylinder phantom, which is developed by before research [22]. The static images of conductivity distribution are reconstructed by the modified Newton-Raphson iterative algorithm. By comparing the imaging results using eigenvalue threshold regularization [14] and truncated SVD, respectively, the former is selected to deal with the next test.

2. Materials and methods

2.1. Data acquisition system

The data acquisition system is developed by our group. This system drives by currents and voltages data are measured. The frequency of stimulating currents is 47 KHz, whose amplitude is from 0.16 mA to 2.56 mA. The precision of the voltage measurement is less than 0.5%.

2.2. Physical phantom

The physical phantom is a cylinder tank of 300 mm in inner-diameter, which simulates the human thorax. 32 compound electrodes are dispatched equidistantly on the periphery of the phantom. The background is NaCl solution with different resistivity. The conductivity perturbation objects are agar blocks also with different resistivity. The value of resistivity is calculated by an experiential formula.

2.3. Static reconstruction algorithm

According to least square principle, its resistivity variation can be calculated by the modified Newton-Raphson algorithm [10, 23]:

$$\Delta\rho^k = -\left[\left[V_c'\left(\rho^k\right)\right]^T V_c'\left(\rho^k\right)\right]^{-1}\left[V_c'\left(\rho^k\right)\right]^T\left[V_c\left(\rho^k\right) - V_m\right] \tag{1}$$

Where, ρ^k is the presumed resistivity distribution of k-th iteration step, $V_c(\rho^k)$ is the forward calculated boundary voltages corresponding to ρ^k, $V_c'(\rho^k)$ is the derivative of $V_c(\rho^k)$ with respect to ρ^k and is called Jacobian matrix, $[V_c'(\rho^k)]^T V_c(\rho^k)$ is called Hessian matrix. Then, the next impedance distribution can be obtained by

$$\rho^{k+1} = \rho^k + \Delta\rho^k \tag{2}$$

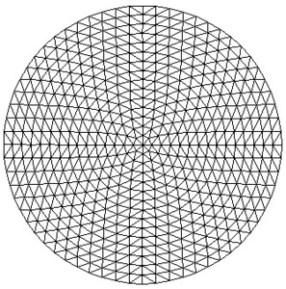

Fig. 1. Reconstructed model.

The iterative stop condition is $\Phi(\rho) \leq 10^{-10}$ or the number of iterative steps is more than some preset number.

2.4. Regularization methods

However, the condition number of Hessian matrix is very large. So, $\Delta\rho^k$ is very sensitive to small error or noise. In order to attenuate the ill-conditioning of the problem, it is a feasible method to reduce the condition number of Jacobian or Hessian matrix. As the condition number of Hessian matrix is the square of that of Jacobian matrix, the Hessian matrix is the main object.

Because known eigenvalues of a matrix can calculate its condition number, the eigenvalues of Hessian matrix can directly adjust the condition number. The eigenvalues of Hessian matrix is solved by the singular value decomposition (SVD). Two kinds of methods are selected to compare the imaging result. One is the eigenvalue threshold regularization (ETR). ETR can easily control the condition number of Hessian matrix by adjusting its regularization parameter. Another is the truncated SVD [13].

2.5. Finite element model

The following finite element model is applied to reconstruct the conductivity distribution, see Figure 1. The model is a 15-layer concentric circle. The whole region is discretized into 1016 triangle elements with 541 nodes. The above grid is also the model of the forward problem when calculating the $V_c(\rho^k)$ in Eq. (1).

3. Results

3.1. Comparison of images using two regularization methods

A series of images using ETR and truncated SVD, respectively, are reconstructed, see Figures 2-5. Two cylinder targets with 66mm diameter are symmetric about the center of the tank. The resistivities of the upper target, the lower target, and the background solution are 2.0 Ωm, 1.0 Ωm and 4.0 Ωm, respectively. The distance between the two targets' boundary increases by 20mm increment. Let the regularization parameter as 1.0×10^6. Graybar ranges from 0 to 255, whose upper number is the maximum resistivity, and the lower is the minimum resistivity.

When the distance is 20 mm, see Figure 2, the image reconstructed by ETR can be distinguished as two objects if taking into account the error in the center. But, the image reconstructed by truncated

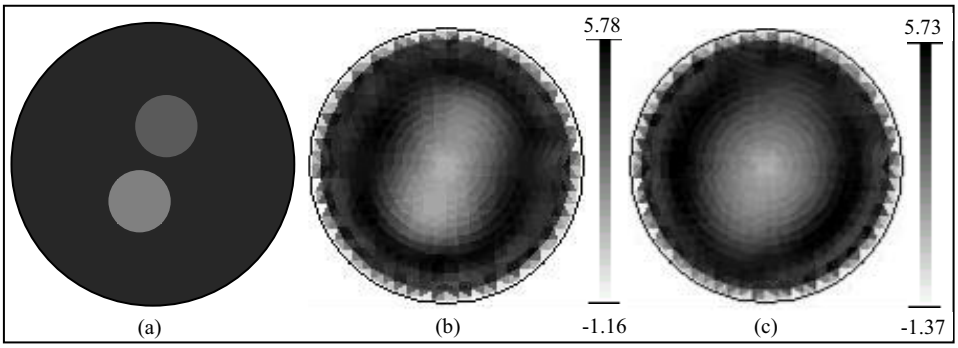

Fig. 2. Static reconstruction imaging of two targets with 20 mm distance. (a) sketch map of targets. (b) reconstruction image using ETR. (c) reconstruction image using truncated SVD.

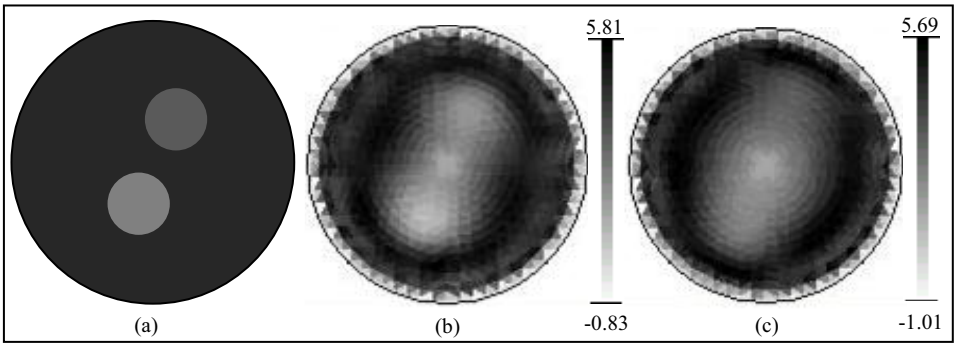

Fig. 3. Static reconstruction imaging of two targets with 40 mm distance. (a) sketch map of targets. (b) reconstruction image using ETR. (c) reconstruction image using truncated SVD.

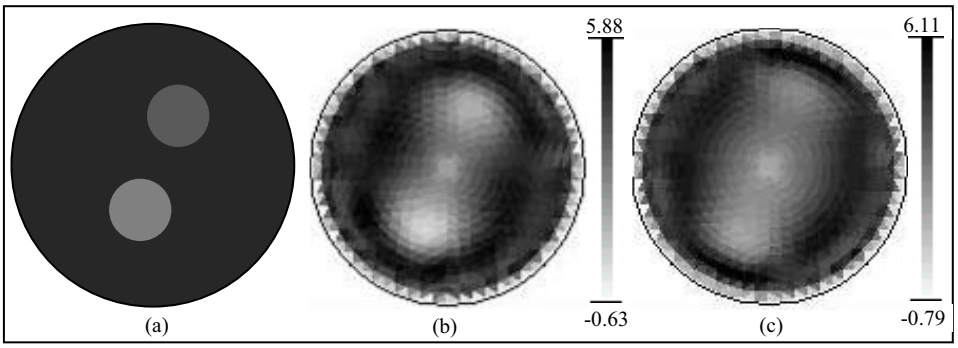

Fig. 4. Static reconstruction imaging of two targets with 60 mm distance. (a) sketch map of targets. (b) reconstruction image using ETR. (c) reconstruction image using truncated SVD.

SVD entirely becomes one object. As the distance increasing, the images made by two methods are all improved step by step, see Figures 3-5. However, the images using ETR are clearer than those using truncated SVD. Therefore, the ETR obtains better reconstruction images than the truncated SVD, especially to the objects near the center.

3.2. Images of complex objects

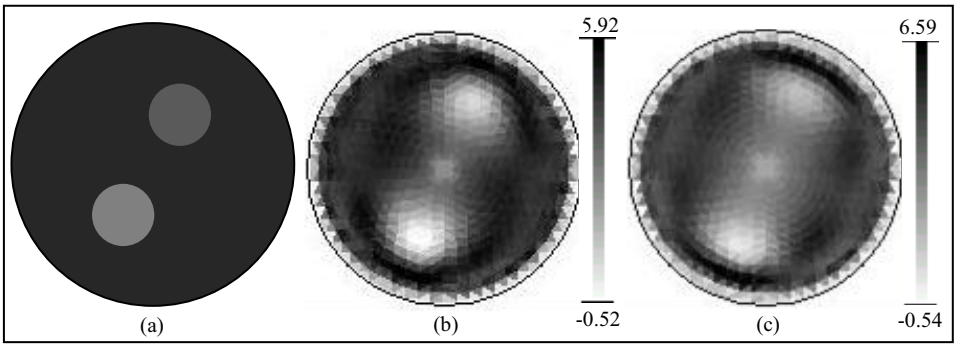

Fig. 5. Static reconstruction imaging of two targets with 80 mm distance. (a) sketch map of targets. (b) reconstruction image using ETR. (c) reconstruction image using truncated SVD.

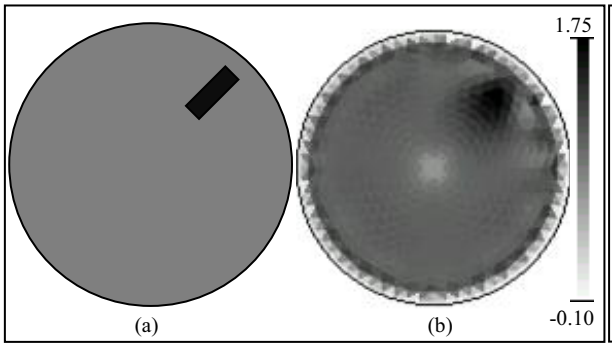

Fig. 6. Static reconstruction imaging of rectangle target. (a) sketch map of 60 mm×20 mm rectangle cylinder with 8.0 Ωm resistivity. The background's resistivity is 1.0 Ωm. (b) reconstruction image using ETR.

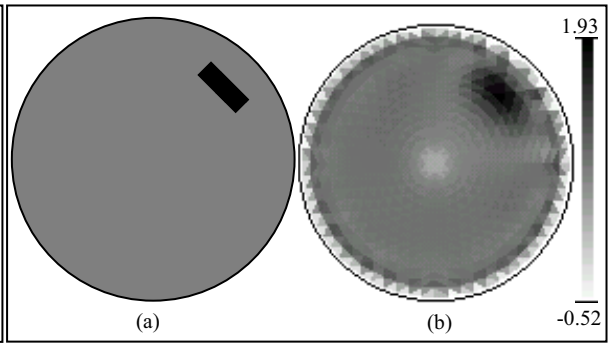

Fig. 7. Static reconstruction imaging of rectangle target. (a) sketch map of 60 mm×20 mm rectangle cylinder with 8.0 Ωm resistivity. The background's resistivity is 1.0 Ωm. (b) reconstruction image using ETR.

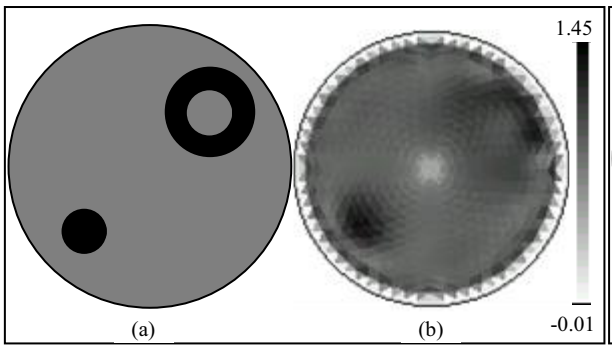

Fig. 8. Static reconstruction imaging of hollow target. (a) sketch map of targets. The upper target is a hollow cylinder with 70 mm inner diameter, 102 mm outer diameter, and 4.0 Ωm resistivity. The lower target is a cylinder with 48 mm diameter and 4.0 Ωm resistivity. The background's resistivity is 1.0 Ωm. (b) the reconstruction image using ETR.

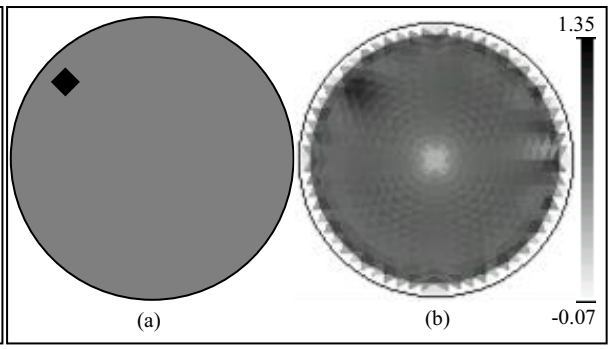

Fig. 9. Static reconstruction imaging of small target. (a) sketch map of 20 mm×20 mm square cylinder with 8.0 Ωm resistivity. The background's resistivity is 1.0 Ωm. (b) reconstruction image using ETR.

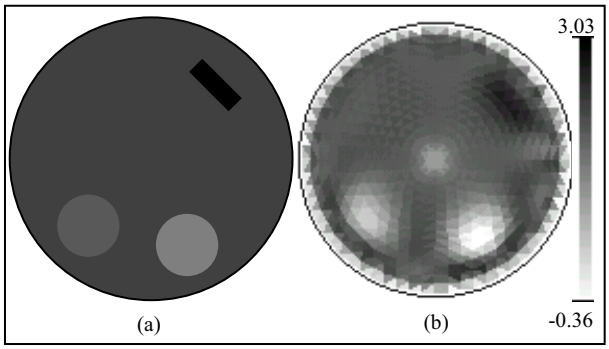

Fig. 10. Static reconstruction imaging of three targets. (a) sketch map of targets. The upper target is a 60 mm×20 mm rectangle cylinder with 8.0 Ωm resistivity. The lower-left target is a cylinder with 66mm diameter and 1.5 Ωm resistivity. The lower-right target is a cylinder with 66mm diameter and 1.0 Ωm resistivity. The background's resistivity is 2.0 Ωm. (b) reconstruction image using ETR.

A group of reconstructed images, see Figures 6-10, are obtained using ETR and measurement data from physical phantom. In the following reconstruction images, set $rc=1.0\times10^{6}$, which is selected by experience. Graybar ranges from 0 to 255, whose upper number is the maximum resistivity, and the lower is the minimum resistivity.

4. Discussions

The ETR can improve the reconstructed results by modifying the eigenvalues of the Hessian matrix. The bigger eigenvalues of Hessian matrix reflect the characteristic of the field near the boundary and the smaller eigenvalues reflect the characteristic of the field near the center, noise and calculating errors. By enlarging the smaller eigenvalues appropriately, not discarding them, the ETR can obtain better reconstruction images than the truncated SVD, especially to the field near the center.

Some shapes of the conductivity perturbation objects in the reconstructed images deform, such as, slim rectangle in Figure 6, and hollow cylinder in Figure 8. But, the reconstruction image of the same slim rectangle in Figure 6 makes a great change. One of the reasons may be the distance close to the boundary of the tank. Another reason is that the size of the triangle element in the finite element model is not enough small.

The positions of perturbation objects in all of the images are correct. When the objects are near to the boundary of tank, the size of objects is nearly equal to their real size. The best distinguishability is about 20/300=6.7% of the tank's diameter, see Figure 9. While the objects are close to the center of the tank, the size of objects is bigger than their real size.

Although the values of the conductivities of the perturbation objects in all of the images are not the precise setup values, the difference of the conductivities of the background solution and the perturbation objects is correct. For example, in Figure 10, four kinds of conductivities are expressed by four kinds of gray colors. Relative to the resistivity of background solution, the minimum resistivity variation, 25%, occurs in Figure 10.

There still exists some reconstructed error in the images, such as the field in the center and the boundary of the reconstruction images. The discretization of the reconstruction FEM model may be one of reasons.

5. Conclusions

Using a data acquisition system with 32 compound electrodes and Newton-Raphson reconstruction algorithm, a series of static images of electrical impedance tomography on physical phantom are reconstructed. Compared to the imaging results on physical phantom with two kinds of regularization methods, ETR can get better results than truncated SVD. Moreover, when setting some complex conductivity perturbation objects, including slim rectangle, hollow cylinder, small rectangle, and three cylinders with different conductivities, the ETR still works. The imaging results can show correct position, size, the conductivity difference, and similar shapes of the perturbation objects.

Acknowledgment

The research work was supported by National Natural Science Foundation of China under Grant No. 61271101 and 12th Five-Year Medical Science Project under Grant No. BWS11Z011.

References

[1] F. Fu, B. Li, M. Dai, S. Hu, X. Li, C. Xu, B. Wang, B. Yang, M. Tang, X. Dong, Z. Fei and X. Shi, Use of electrical impedance tomography to monitor regional cerebral edema during clinical dehydration treatment, PLoS One **9** (2014), e113202.

[2] M. Dai, B. Li, S. Hu, C. Xu, B. Yang, J. Li, F. Fu, Z. Fei and X. Dong, In vivo imaging of twist drill drainage for subdural hematoma: A clinical feasibility study on electrical impedance tomography for measuring intracranial bleeding in humans, PLoS One **8** (2013), e55020.

[3] Z. Zhao, R. Fischer, I. Frerichs, U. Müller-Lisse and K. Möller, Regional ventilation in cystic fibrosis measured by electrical impedance tomography, Journal of Cystic Fibrosis **11** (2012), 412–418.

[4] J. Schramel, C. Nagel, U. Auer, F. Palm, C. Aurich and Y. Moens, Distribution of ventilation in pregnant Shetland ponies measured by electrical impedance tomography, Respiratory Physiology & Neurobiology **180** (2012), 258–262.

[5] M. Balleza-Ordaz, E. Perez-Alday, M. Vargas-Luna and J.P. Riu, Tidal volume monitoring by electrical impedance tomography (EIT) using different regions of interest (ROI): Calibration equations, Biomedical Signal Processing and Control **18** (2015), 102–109.

[6] M. Leinonen, H. Hakula and N. Hyvönen, Application of stochastic Galerkin FEM to the complete electrode model of electrical impedance tomography, Journal of Computational Physics **269** (2014), 181–200.

[7] P.D. Ledger, Hp-finite element discretisation of the electrical impedance tomography problem, Computer Methods in Applied Mechanics and Engineering **225**–**228** (2012), 154–176.

[8] M.A. Heravi, L. Marin and C. Sebu, The method of fundamental solutions for complex electrical impedance tomography, Engineering Analysis with Boundary Elements **46** (2014), 126–139.

[9] P.G. Daneshmand and R. Jafari, A 3D hybrid BE–FE solution to the forward problem of electrical impedance tomography, Engineering Analysis with Boundary Elements **37** (2013), 757–764.

[10] T.J. Yorkey, J.G. Webster and W.J. Tompkins, Comparing reconstruction algorithms for electrical impedance tomography, IEEE Transaction on Biomedical Engineering **34** (1987), 843–852.

[11] Q. Wang, H. Wang, Z. Cui and C. Yang, Reconstruction of electrical impedance tomography (EIT) images based on the expectation maximum (EM) method, ISA Transactions **51** (2012), 808–820.

[12] J. Wang, J. Ma, B. Han and Q. Li, Split Bregman iterative algorithm for sparse reconstruction of electrical impedance tomography, Signal Processing **92** (2012), 2952–2961.

[13] P. Hua, E.J. Woo and J.G. Webster, Iterative reconstruction methods using regularization and optimal current patterns in electrical impedance tomography, IEEE Transaction on Biomedical Engineering **10** (1991), 621–628.

[14] R. Liu, Y. Li, F. Fu, F. You, X. Shi and X. Dong, Time-difference imaging of magnetic induction tomography in three-layer brain physical phantom, Measurement Science and Technology **25** (2014), 065402.

[15] J. Nasehi Tehrani, A. McEwan, C. Jin and A. Schaik, L1 regularization method in electrical impedance tomography by using the L1-curve (Pareto frontier curve), Applied Mathematical Modelling **36** (2012), 1095–1105.

[16] S.B. Ayati, K. Bouazza-Marouf and D. Kerr, In vitro localisation of intracranial haematoma using electrical impedance tomography semi-array, Medical Engineering & Physics **37** (2015), 34–41.
[17] D. Chakraborty and M. Chattopadhyay, Finite element method based modeling of a sensory system for detection of atherosclerosis in human using electrical impedance tomography, Procedia Technology **10** (2013), 262–270.
[18] J.B. Li, C. Tang, M. Dai, G. Liu, X. Shi, B. Yang, C. Xu, F. Fu, F. You, M. Tang and X. Dong, A new head phantom with realistic shape and spatially varying skull resistivity distribution, IEEE Transaction on Biomedical Engineering **61** (2014), 254–263.
[19] T.K. Bera, S.K. Biswas, K. Rajan and J. Nagaraju, Projection Error Propagation-based Regularization (PEPR) method for resistivity reconstruction in electrical impedance tomography (EIT), Measurement **49** (2014), 329–350.
[20] B. Yang, X. Shi, M. Dai, C. Xu, F. You, F. Fu, R. Liu and X. Dong, Real-time imaging of cerebral infarction in rabbits using electrical impedance tomography, Journal of International Medical Research **42** (2014), 173–183.
[21] C. Xu, M. Dai, F. You, X. Shi, F. Fu, R. Liu and X. Dong, An optimized strategy for real-time hemorrhage monitoring with electrical impedance tomography, Physiological Measurement **32** (2011), 585–598.
[22] X. Shi, X. Dong, F. You, F. Fu and R. Liu, High precision multifrequency electrical impedance tomography system and preliminary imaging results on saline tank, Proceeding of 27th Annual International Conference of the IEEE Engineering in Medicine and Biology Society, Shanghai, 2005, pp. 1492–1495.
[23] E.J. Woo, P. Hua and J.G. Webster, A robust image reconstruction algorithm and its parallel implementation in electrical impedance tomography, IEEE Transaction on Biomedical Engineering **12** (1993), 137–146.